PAPER

Evolution of high-frequency Raman modes and their doping dependence in twisted bilayer MoS$_2$†

Rahul Debnath,*‡[a] Indrajit Maity, [ID] *‡[a] Rabindra Biswas,[b] Varun Raghunathan,[b] Manish Jain[a] and Arindam Ghosh[a,c]

Twisted van der Waals heterostructures provide a new platform for studying strongly correlated quantum phases. The interlayer coupling in these heterostructures is sensitive to the twist angle (θ) and key to controllably tuning several interesting properties. Here, we demonstrate the systematic evolution of the interlayer coupling strength with twist angle in bilayer MoS$_2$ using a combination of Raman spectroscopy and classical simulations. At zero doping, we observe a monotonic increase in the separation between the A$_{1g}$ and E$_{2g}^1$ mode frequencies as θ decreases from $10° \rightarrow 1°$, and the separation approaches that of a bilayer at small twist angles. Furthermore, using doping dependent Raman spectroscopy, we reveal the θ dependent softening and broadening of the A$_{1g}$ mode, whereas the E$_{2g}^1$ mode remains unaffected. Using first principles based simulations, we demonstrate large (weak) electron–phonon coupling for the A$_{1g}$ (E$_{2g}^1$) mode, which explains the experimentally observed trends. Our study provides a non-destructive way to characterize the twist angle and the interlayer coupling and establishes the manipulation of phonons in twisted bilayer MoS$_2$ (twistnonics).

[a]*Department of Physics, Indian Institute of Science, Bangalore 560012, India. E-mail: rahuldebnath@iisc.ac.in, indrajit@iisc.ac.in*

[b]*Department of Electrical and Communication Engineering, Indian Institute of Science, Bangalore 560012, India*

[c]*Centre for Nano Science and Engineering, Indian Institute of Science, Bangalore 560012, India*

†Electronic supplementary information (ESI) available. See DOI: 10.1039/C9NR09897F

‡Contributed equally to this work.

1. Introduction

The choice of the material, the number of layers and the relative rotation between the layers (twist) provide three important degrees of freedom for engineering the properties of van der Waals (vdW) heterostructures.[1–7] The introduction of a twist between two layers of a two dimensional material generates a large-scale periodic pattern, known as a moiré superlattice. In the case of twisted bilayer graphene, the moiré superlattice potentially induces a periodic pattern in the electrons, which yields many fascinating phenomena, such as flat bands in the electronic band structure which can host a correlated insulating phase,[8] superconductivity,[9,10] and ferromagnetism.[11] The ability to tune these properties in a controlled manner requires a detailed understanding of the evolution of interlayer coupling strength with twisting.[10,12–14]

Compared to graphene, the effects of twisting in layered MoS$_2$, an important material for electronic and optoelectronic applications,[2,4,5] have been relatively less explored.[15–32] The existing experimental studies have predominantly concentrated on the change in optical properties and low frequency vibrational modes using chemical vapor deposition (CVD) grown samples.[15–22] Although the change in the interlayer coupling strength with twist angle is evident in these studies, a definitive experiment relating the precise evolution of the interlayer coupling strength to the twist angle is still lacking.

Electron–phonon coupling (EPC) affects many important properties in solids, including those in two dimensional atomic layers, for instance carrier mobility, and thermalization of hot carriers.[33] Doping dependent Raman spectroscopy is often used to probe EPC in two dimensional materials.[34–39] The evolution of the Raman active modes upon electron doping in twisted bilayers of transition metal dichalcogenides (TMDCs) can shed light on the twist angle dependence of EPC. As the electron mobility in 2D TMDC devices is often limited by electron–phonon interactions,[33] by tuning the EPC through the twist angle one can, in principle, engineer the mobility in these systems.

Here, using bilayer MoS$_2$, a prototypical TMDC, we investigate the evolution of the high-frequency phonon modes as a function of twist angle and electron doping using Raman spectroscopy. The twisted structures are prepared from mechanically exfoliated MoS$_2$ layers, which exhibit higher mobility and lower disorder than CVD grown samples.[40] We demonstrate a monotonic change in the E$_{2g}^1$ and A$_{1g}$ modes for relatively small twist angles ($\theta \lesssim 10°$) by combining Raman spectroscopy

with classical and first principles based simulations. We also find two intriguing features of the electron doping dependence of these high-frequency modes. First, irrespective of the number of layers (single or bilayer) or the twist angle between them, the A_{1g} mode shows strong doping dependence; the phonon frequency decreases by ~ 0.9 cm^{-1} and the linewidth increases by ~ 2 cm^{-1} for electron doping of 4.87×10^{12} cm^{-2} at large twist angle. On the other hand, the phonon frequency and linewidth of the E_{2g}^1 mode remain unchanged on electron doping. Second, the doping dependence of the A_{1g} mode frequencies for large (small) twist angles resembles that of a single layer (bilayer), thereby providing a new route to identify the twist angle and doping concentration in twisted bilayer MoS$_2$ (tBLMoS$_2$). We explain these observations using first principles based calculations.

2. Materials and methods

2.1. Experimental details

2.1.1. Device fabrication. Atomically thin crystalline layers of MoS$_2$ were prepared by standard mechanical exfoliation of MoS$_2$ on 285 nm thick SiO$_2$ on a p^{++}-doped Si substrate using the scotch tape technique.[41,42] We used the dry transfer[5] method to stack two mechanically exfoliated MoS$_2$ layers to prepare twisted bilayer samples (tBLMoS$_2$). By using a micromanipulation stage, this method allows the preparation of samples with the desired twist angle within the accuracy of 1°. Additionally, this technique greatly reduces any contamination between the two layers, which ensures robust and reproducible device properties. Fig. 1a and b show a generic moiré pattern

due to twisting and an illustrative micrograph of tBLMoS$_2$ after transfer on the SiO$_2$/Si^{++} substrate, respectively. Edge profiles of the top and bottom MoS$_2$ layers were determined using the technique described in ref. 43. Among 2D materials, MoS$_2$ shows a distinctive tendency to cleave along the zigzag direction. For each exfoliated monolayer flake, the angle between the two straight edges (edge angle) was measured, and those with edge angles of $\approx 60°$ were chosen. To make tBLMoS$_2$ devices, we used MoS$_2$ monolayers with smooth straight edges. Here the twist angle is defined as the relative rotation between the straight edges of the top and bottom flakes determined by using optical microscopy. Based on this definition, we mostly fabricated twisted devices with $\theta \to 0°$, and a few devices with $\theta \to 60°$. We also carried out second harmonic polarization measurements at several twist angles. This gave us a non-destructive way to verify the twist angle within an experimental error of $\pm 1°$ (see ESI, Fig. S6†). Electrical contacts were fabricated by e-beam lithography, followed by 5/50 nm Cr/Au deposition. The room temperature gate voltage dependent Raman measurements were performed with 532 nm laser excitation under high vacuum (10^{-5} mbar). The laser power was kept below 1.5 mW to avoid sample heating. For gating, we used a 285 nm SiO$_2$ back gate. The threshold voltage (V_{Th}), at which the device switches from the off state to the on state was determined (see ESI, Fig. S3†). The effective electron doping concentration was determined using the equation $n*e = C_{ox}(V_g - V_{Th}) = C_{ox}\tilde{V}_g$, where C_{ox} is the gate capacitance per unit area (here 1.2×10^{-4} F m^{-2}). The maximum electron doping that we studied in this work was $\sim 0.004e$ per unit cell at $\tilde{V}_g = 60$ V.
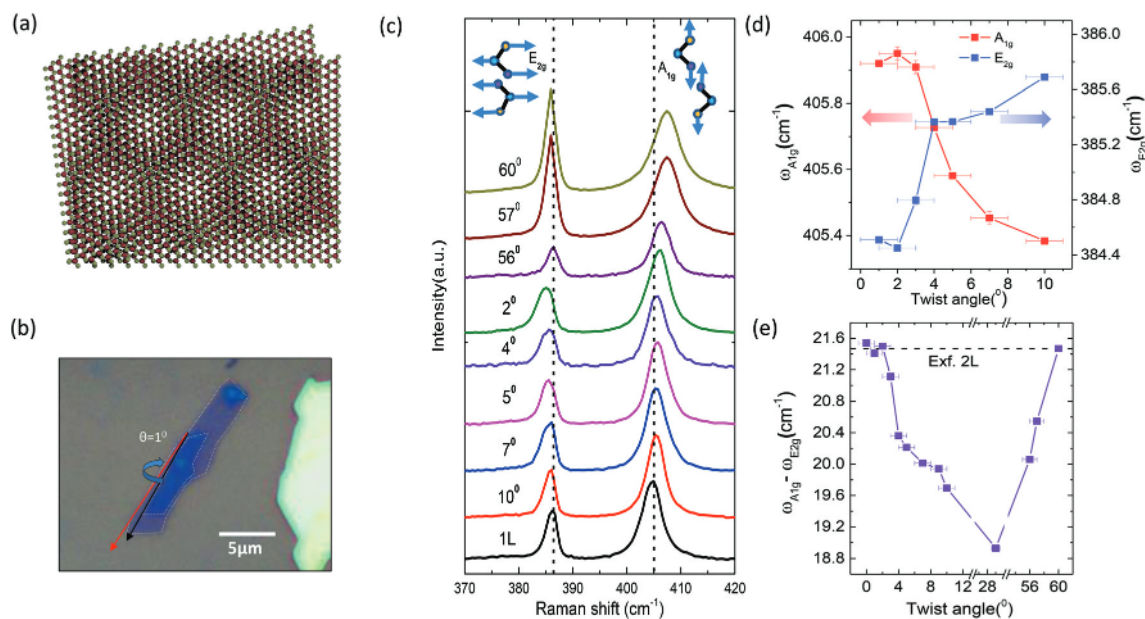

Fig. 1 (a) Schematic of a generic moiré pattern. (b) Optical micrograph of twisted bilayer MoS$_2$ with the twist angle defined as the relative rotation between two straight edges. (c) Raman spectra of monolayer MoS$_2$ and bilayer MoS$_2$ with the dashed lines representing the phonon modes of monolayer MoS$_2$. (d) and (e) Twist angle dependence of the individual E_{2g}^1 and A_{1g} mode frequencies and their peak separation, respectively. The dashed black line shows the peak separation of naturally exfoliated bilayer MoS$_2$. The error bars show the uncertainty in θ and the peak position.

2.1.2. Dry transfer method. MoS_2 flakes were exfoliated on different $SiO_2/(p^+)Si$ substrates. A drop of PDMS polymer was placed on a transparent glass slide and baked at 150 °C for 30 min. We used LCC polymer for the sacrificial layer, which was spin coated on the PDMS drop at 8000 rpm and baked for 3 h. The glass slide containing the PDMS drop, facing down, was aligned with the substrate containing the flake under the microscope. Using a micro-manipulator, the alignment was performed in such a way that, when the glass slide and the substrate were brought closer, the convex surface of the LCC only touched the substrate in the region surrounding the flake. Following a contact time of 5 min at 57 °C, the glass slide was removed, lifting the flake from the substrate due to the strong adhesion to LCC. To avoid the deformation of LCC and tearing the flake, the lower substrate temperature was decreased to 50 °C before detaching the LCC. In the next step, the LCC drop, containing the upper layer flake, was precisely and manually aligned with the bottom flake at the desired twist angle by using the micro-manipulator, and then picked up in a similar manner to form the heterostructure. In the final step, the glass slide containing the LCC, along with the heterostructure, was pressed against an RCA cleaned patterned $SiO_2/(p^+)Si$ substrate at 120 °C. The desired heterostructure stuck to the patterned $SiO_2/(p^+)Si$ substrate along with part of the LCC. Later, the LCC was dissolved in acetone to obtain the heterostructure on the patterned $SiO_2/(p^+)Si$ substrate.

2.1.3. Raman spectroscopy. Raman spectra of MoS_2 flakes were recorded by using a Horiba LabRAM HR spectrometer. A 532 nm laser with laser power less than 1.5 mW was used for the spectroscopy measurements. For gate voltage dependent Raman spectroscopy, a vacuum compatible (10^{-5} mbar) chamber was used.

2.2. Details of the theoretical calculations

2.2.1. Classical simulations. We use the Twister code[23] to create twisted bilayer MoS_2 with several commensurate twist angles. The commensurate twist angles and corresponding moiré lattice constants are calculated in the following manner:

$$\theta = \cos^{-1}\left(\frac{m^2 + 4mn + n^2}{2(m^2 + mn + n^2)}\right), \text{ and } L_m = \frac{|m-n|a}{2\sin(\theta/2)}, \text{ where } m$$

and n are integers and a is the lattice constant for the unit cell of MoS_2. The smallest moiré lattice constants are only found for $|m - n| = 1$, which is feasible to simulate. We use the Stillinger–Weber and Kolmogorov–Crespi potentials to capture the intralayer and interlayer interactions, respectively.[44–46] The phonon frequencies are calculated for relaxed tBLMoS$_2$ using PHONOPY.[47]

2.2.2. First principles calculations. The first principles based quantum calculations using density functional theory[48,49] are performed with both the local density approximation (LDA) and the Perdew–Burke–Ernzerhof generalized gradient approximation (GGA) for the exchange–correlation functional as implemented in Quantum ESPRESSO.[50] We use a plane wave basis set with a kinetic energy cutoff of 80 Ry, an optimized norm conserving Vanderbilt pseudopotential,[51] and

a $12 \times 12 \times 1$ uniform $\vec{k}$ point Monkhorst–Pack grid for the sampling of the Brillouin zone with a 30 Å vacuum. For the GGA, we use GGA + DFT-D[52] for the BLMoS$_2$ calculations. For the linewidth calculations, we compute the phonon frequencies and eigenvectors using a $6 \times 6 \times 1$ uniform $\vec{q}$ point grid and determine maximally localized Wannier functions[53,54] with a much finer electron grid ($72 \times 72 \times 1\vec{k}$) and phonon grid ($72 \times 72 \times 1\vec{q}$) to interpolate the electron–phonon coupling matrix elements with EPW.[55,56] The linewidth is finally calculated from the imaginary part of the phonon self-energy using EPW with 10^6 $\vec{k}$ points. In the double delta approximation, the smearing used to replace the delta function is chosen to be relatively large (0.1 eV). The electron doping for the linewidth calculations is simulated within the rigid band approximation by shifting the Fermi level above the conduction band minimum. The Fermi level is determined with EPW by adding a fraction of electrons to the unit cell and using a fine $1000 \times 1000 \times 1\vec{k}$ grid with a small smearing of ~0.002 eV to replace the energy conserving delta function.

For the doping dependent phonon calculations (at Γ), we explicitly add a small fraction of electrons, corresponding to the gate voltage in our experiment. For single layer MoS_2 (SLMoS$_2$), we use a dense $96 \times 96 \times 1\vec{k}$ grid and a smearing of 0.002 Ry, corresponding to room temperature. To correct the boundary conditions for 2D materials, we also compute the phonon mode frequencies by truncating the Coulomb interaction in the out-of-plane direction of SLMoS$_2$. We do not see significant changes on renormalization of the phonon mode frequencies. Spin–orbit coupling is not included in our calculations.

3. Results and discussion

3.1. Experiments

3.1.1. θ dependence of high-frequency modes without doping. To investigate the twist angle dependence of the interlayer interaction in tBLMoS$_2$, we measured the Raman spectra of tBLMoS$_2$ for several twist angles (Fig. 1c) with a focus on the two prominent first-order vibrational modes, the in-plane E_{2g}^1 mode and the out-of-plane A_{1g} mode. It should be noted that the E_{2g}^1 mode is red-shifted and the A_{1g} mode is blue-shifted as we increase the layer number from monolayer to bilayer MoS_2.[57,58] As is well known, the blue-shift of the A_{1g} mode with increasing layer number is due to additional "springs" between two neighboring MoS_2 layers, whereas the red-shift of the E_{2g}^1 mode frequencies arises from enhanced dielectric screening of the Coulomb interaction.[58] The high-symmetry stacking regions present in tBLMoS$_2$ are different for $\theta \to 0°$, and $\theta \to 60°$. This is due to the presence of different sub-lattice atoms (Mo, S) in the unit cell.[23,26] Therefore, there is a quantitative difference in the position and width of the E_{2g}^1 mode near $\theta = 0°$ and $\theta = 60°$. Here, we mainly focus on twist angles near 0°. Among all the possible stacking modes, AA′ stacking ($\theta = 60°$, Mo and S of the top layer are directly above S and Mo of the bottom layer) is known to be the most stable. As

a result, naturally exfoliated BLMoS$_2$ has AA' stacking. In Fig. 1d, we show the evolution of the E$_{2g}^1$, and A$_{1g}$ mode frequencies with twist angle. It is clear that as θ decreases (from $10° \rightarrow 1°$) the E$_{2g}^1$ mode is red-shifted while the A$_{1g}$ mode is blue-shifted monotonically. The separation between these peaks ($\omega_{A_{1g}} - \omega_{E_{2g}^1}$) is often used as a quantitative measure of the strength of the interlayer mechanical coupling.[17] For brevity, we refer to the interlayer mechanical coupling as the interlayer coupling. The larger the peak separation, the stronger the interlayer coupling. For example, we find that the peak separation of BLMoS$_2$ ($\sim$21.3 cm^{-1}) is always larger than that of SLMoS$_2$ ($\sim$18.7 cm^{-1}). Remarkably, we discover that the peak separation can be monotonically tuned by altering the twist angle in tBLMoS$_2$ (Fig. 1e). The peak separation is a maximum for $\theta \lesssim 2°$ (approaches the BLMoS$_2$ value) and a minimum for $\theta \sim 10°$ (slightly greater than the SLMoS$_2$ value). This immediately implies tunability of the interlayer coupling strength through altering the twist angle. Moreover, it also suggests that tBLMoS$_2$ with small (large) twist angle behaves like BLMoS$_2$ (SLMoS$_2$).

3.1.2. θ dependence of high-frequency modes with doping.

Next, we investigate the evolution of the high-frequency phonon modes in tBLMoS$_2$ upon electron doping. A schematic and micrograph of the tBLMoS$_2$ device used in this experiment are shown in Fig. 2a and b, respectively. In Fig. 2c, we show the gate voltage dependence of the A$_{1g}$ and E$_{2g}^1$ modes for a 7°

twist angle. It is evident from the figure that, as the gate voltage increases, the A$_{1g}$ mode is softened and broadened, whereas the E$_{2g}^1$ mode remains unaffected. In Fig. 2d and e (Fig. 2g and h), we show the shift of the A$_{1g}$ (E$_{2g}^1$) mode frequency and the corresponding linewidth respectively, as a function of electron doping at different twist angles. Three Lorentzians are fitted to the data to obtain the line shape parameters, where the peak position and full width at half maximum (FWHM) denote the phonon frequency and linewidth, respectively (see ESI, Fig. S2†). Here, $\Delta\omega$ and ΔFWHM signify the shift of the mode frequency and FWHM with respect to zero doping (for instance, $\Delta\omega = \omega(\tilde{V}_g \neq 0) - \omega(\tilde{V}_g = 0)$). We find that the softening of the A$_{1g}$ mode of BLMoS$_2$ under electron doping is smaller compared to that of SLMoS$_2$. This can be qualitatively understood by noting that, upon electron doping, different conduction valleys with different band curvature are occupied in SLMoS$_2$ and BLMoS$_2$ (K for the monolayer, Λ for the bilayer as shown in Fig. 2i, see ESI, Fig. S4† for details). The rate of softening of the A$_{1g}$ mode with $\tilde{V}_g$ is shown in Fig. 2f for different twist angles. For large θ ($\approx$7°), the slope of the softening of the A$_{1g}$ mode frequencies ($\sim$−0.016 cm^{-1} V^{-1}) is identical to that of SLMoS$_2$. This further suggests that the two layers are very weakly coupled for large twist angles. As $\theta \rightarrow 0°$ ($\theta \lesssim 2°$), the softening of the A$_{1g}$ mode resembles that of BLMoS$_2$. In sharp contrast to the A$_{1g}$ mode, the phonon frequencies of the E$_{2g}^1$ mode remain unaffected
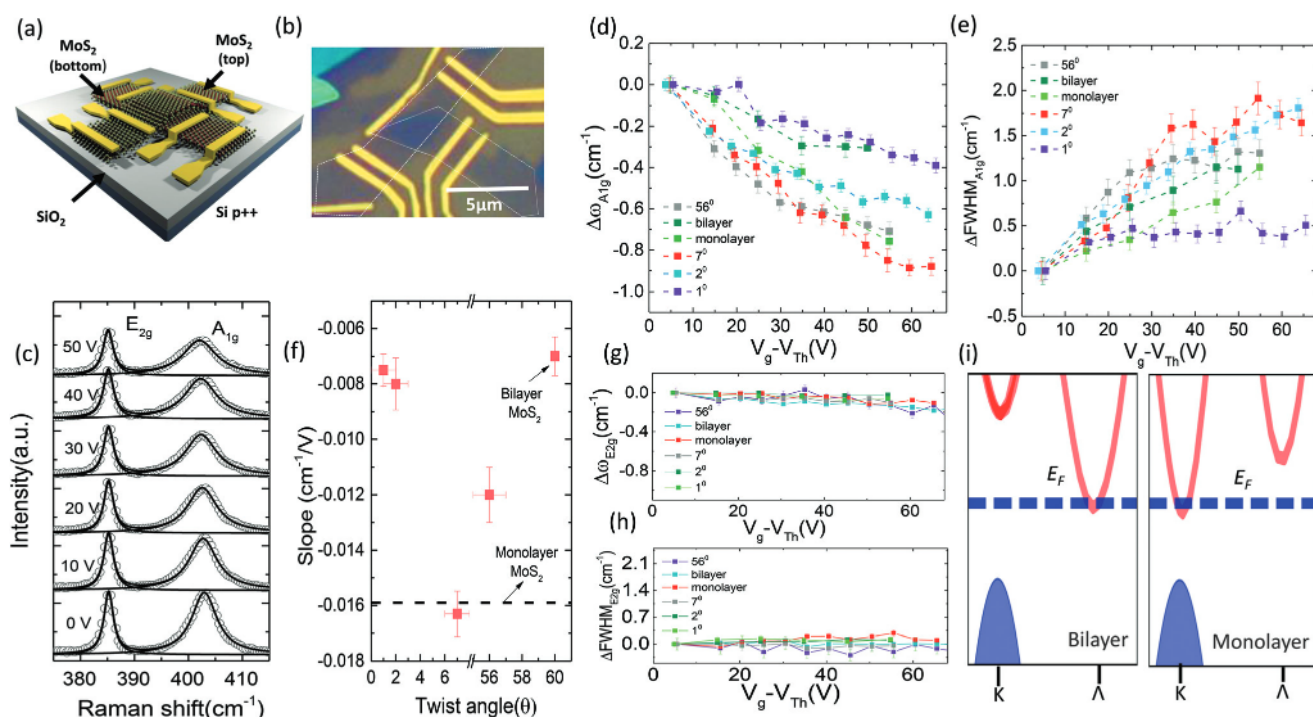

Fig. 2 (a) Schematic of the tBLMoS$_2$ FET device. (b) Optical micrograph of tBLMoS$_2$ ($\theta = 56°$). (c) Raman spectra of tBLMoS$_2$ for $\theta = 7°$ at different gate voltages. (d) and (g) The gate voltage dependence of the softening of the A$_{1g}$ and E$_{2g}^1$ mode frequencies, respectively. (e) and (h) The gate voltage dependence of the broadening (linewidth) of the A$_{1g}$ and E$_{2g}^1$ modes, respectively. (f) The slope of the softening of the A$_{1g}$ mode frequency calculated by fitting a straight line to the doping dependent Raman data. (i) Schematic of the Fermi level position showing the occupation of different valleys in monolayer and bilayer MoS$_2$ for the maximum doping considered.
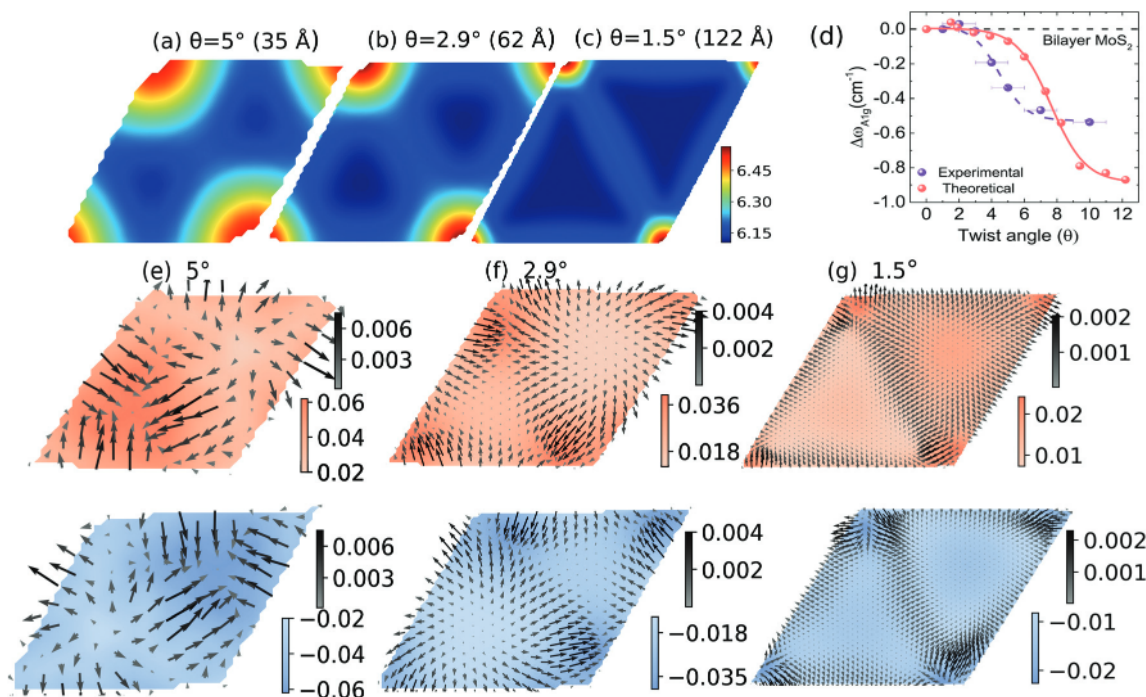
Fig. 3 (a)–(c) Evolution of the ILS landscape of relaxed tBLMoS$_2$ with moiré lattice constants written in brackets. The color bar denotes the ILS in Å. (d) Twist angle dependence of $\Delta\omega_{A_{1g}}$. Both the theoretical and experimental data are fitted with a sigmoid function (see the main text for fitting parameters). (e)–(g) A visualization of the vibrations of the bottom S atoms of the top layer of MoS$_2$ in tBLMoS$_2$, corresponding to the normalized A$_{1g}$ mode for $\theta = 5°$, 2.9° and 1.5°, respectively (top panel). Similarly, the panel below shows the corresponding eigenvectors for the top S atoms of the bottom layer of MoS$_2$. The out-of-plane displacements are denoted by the colored fields, whereas the arrows denote the in-plane displacements.

by electron doping. This is due to large electron–phonon coupling occurring in the A$_{1g}$ mode, which preserves the symmetry of the MoS$_2$ lattice.[36] Our results clearly establish a one-to-one correspondence between the doping concentration and the softening of the A$_{1g}$ mode frequency of tBLMoS$_2$. Furthermore, in Fig. 2e and h, we show that the change in linewidth (ΔFWHM) of the A$_{1g}$ mode in tBLMoS$_2$ increases significantly under electron doping, whereas the linewidth of the E$_{2g}^1$ mode remains unaffected. It should be noted that the changes in ΔFWHM within the applied range of gate voltages are similar for both SLMoS$_2$ and BLMoS$_2$. Interestingly, the change in ΔFWHM for $\theta \approx 1°$ is strikingly different (Fig. 2e). We find that ΔFWHM not only saturates at smaller gate voltages, but also attains an unmistakably smaller maximum than at all the other measured twist angles for $\tilde{V}_g = 60$ V.

3.2. Simulations

3.2.1. θ dependence of the interlayer separation landscape. The introduction of twist in bilayer MoS$_2$ leads to the co-existence of multiple high-symmetry stacking regions in tBLMoS$_2$. To compare with the experimental data, we restrict the theoretical analysis to $\theta \to 0°$. In unrelaxed tBLMoS$_2$ with $\theta \to 0°$, we find two unique high-symmetry stacking regions, AA (where Mo and S of the top layer are directly above Mo and S of the bottom layer) and AB (Bernal stacking with Mo of the top layer directly above S of the bottom layer, the same as BA stacking with S of the top layer directly above Mo of the bottom layer).[59]

Among these stacking modes, AA (AB, BA) stacking is the energetically most unfavorable (favorable).[26,46] Upon relaxing these structures, the most stable stacking regions grow significantly. In order to illustrate this, we show the evolution of the interlayer separation (ILS) landscape in Fig. 3a–c, calculated from the separation between Mo atoms of different MoS$_2$ layers.[26] As θ decreases, the stable AB and BA stacking regions (alternate blue triangles with minimum ILS) occupy significantly larger area-fractions of tBLMoS$_2$ than the unfavorable AA stacking region (red circles with maximum ILS). This twist angle dependence of the ILS landscape inherently controls the evolution of the high-frequency Raman modes.

3.2.2. θ dependence of high-frequency modes. Considering the significantly large cost of phonon calculations using first principles based methods, we adopt classical force field based simulations to compute the A$_{1g}$ mode frequencies for tBLMoS$_2$. In Fig. 3d, we show the evolution of the A$_{1g}$ mode frequencies (with respect to the bilayer A$_{1g}$ mode) for the relevant twist angles in our experiments. The calculated A$_{1g}$ mode is only shown with the largest projection, p$^{A_{1g}}$. The projection is defined as $\langle \hat{e}_{t\text{BLMoS}_2} | \hat{e}_{A_{1g}} \rangle$, where the eigenvectors of tBLMoS$_2$ are projected on the A$_{1g}$ mode of BLMoS$_2$. Our calculations correctly capture the monotonic increase in the A$_{1g}$ mode frequencies as $\theta \to 0°$. Furthermore, we find that both the theoretical and experimental data can be fitted well with a sigmoid curve, $A/(1 + e^{(-(\theta - \theta_0)/d)})$ for $\Delta\omega_{A_{1g}}$ (Fig. 3d). The fitted parameters are also consistent with each other (theoretical: $A =$

-0.88 ± 0.02, $\theta_0 = 7.6 \pm 0.1$, $d = 1 \pm 0.1$; experimental: $A = -0.55 \pm 0.02$, $\theta_0 = 4.5 \pm 0.2$, $d = 0.8 \pm 0.2$). It should also be noted that the experimentally assigned twist angle has an uncertainty of $1°$ (Fig. 3d). In order to understand the twist angle dependence of the A_{1g} mode from a microscopic point of view, we show the eigenvector components on the inter-layer-nearest-neighbor S atoms in tBLMoS$_2$ (Fig. 3e–g). For large θ, the neighboring S atoms from two layers locally move out-of-phase but not with the same amplitude ("incoherent", Fig. 3e). This is due to the presence of multiple high-symmetry stacking regions of equal area-fraction (Fig. 3a), leading to inhomogeneous interlayer coupling.[26] As $\theta \rightarrow 0°$, the neighboring S atoms from two layers locally move out-of-phase and with a similar amplitude ("coherent", Fig. 3g). This is due to the significant increase in the stable AB and BA stacking area as shown in the ILS landscape (Fig. 3c). The amplitudes of the in-plane displacements are always one order of magnitude smaller than those of the out-of-plane displacements. Both the ILS landscape and the evolution of the A_{1g} mode clearly justify the bilayer-like behavior of tBLMoS$_2$ with small twist angles ($\theta \lesssim 3°$) and the single layer-like behavior at large twist angles observed in our experiments.

A similar detailed quantitative estimate of the twist angle dependence of the E_{2g}^1 mode frequencies requires proper treatment of the dielectric screening of the Coulomb interaction.[58] The present parametrization of the classical force field used in our calculations does not properly take into account this screening. Hence, we qualitatively explain the observed trend for the E_{2g}^1 mode using first principles calculations based on density functional perturbation theory (DFPT). Our argument relies on two important observations of the θ dependence of the relaxed ILS landscape: (i) for $\theta \lesssim 3°$, AB/BA stacking occupies a significantly large area-fraction of tBLMoS$_2$ and the ILS for these stacking modes is a minimum (≈ 6.1 Å), and (ii) for relatively large twist angles, both the stable stacking modes not only occupy similar area-fractions to the AA stacking mode but also have a larger ILS ($\gtrsim 6.2$ Å).[26] Thus, by simply noting the change in the E_{2g}^1 mode frequencies for AB stacking on increasing the ILS from the minimum, we can qualitatively understand the θ dependence. We note that the ILS for AB stacking decreases as $\theta \rightarrow 0°$ and reaches its minimum for $\theta \lesssim 3°$.[26] We increase the ILS for AB stacking by ~ 0.3 Å relative to its equilibrium spacing, which causes stiffening of the E_{2g}^1 mode by ~ 0.2 cm^{-1}. In sharp contrast, the A_{1g} mode softens by ~ 3 cm^{-1}. The frequencies of both modes become closer to their single layer values with the increase in ILS. In SLMoS$_2$, the frequency of the E_{2g}^1 (A_{1g}) mode is greater (less) than in BLMoS$_2$.[57,58] Thus, the frequency shifts in tBLMoS$_2$ can be qualitatively understood in terms of the change in the ILS.

3.2.3. Softening and broadening of high-frequency modes due to doping.
The intrinsic linewidth of the phonon modes can have two origins, phonon–phonon anharmonic effects and EPC. In view of our doping dependent Raman measurements, we study only the linewidth change due to EPC. In our calculations of linewidth, the electron doping is modelled in the
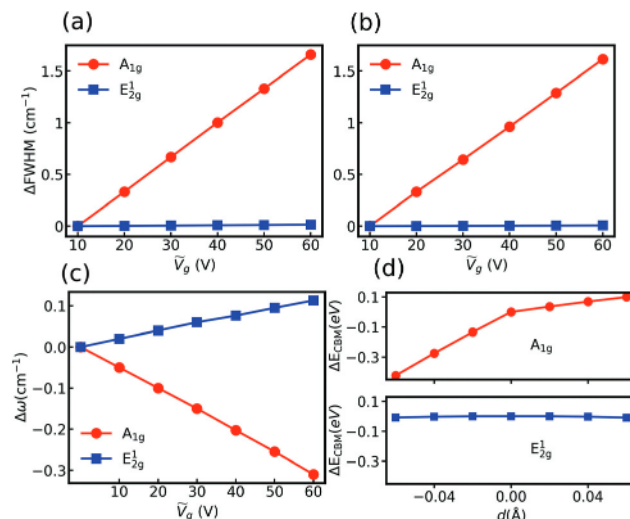

Fig. 4 (a) and (b) The doping dependence of the linewidth of the E_{2g}^1 and A_{1g} modes for single layer and bilayer MoS$_2$, respectively. (c) The doping dependence of the phonon mode frequencies for single layer MoS$_2$. (d) The change in the conduction band minimum at the K point of the electronic band structure due to different phonon modes with several displacement amplitudes (large amplitude is used to show the difference clearly).

rigid band approximation by shifting the Fermi level above the conduction band minimum.[60] In Fig. 4a and b, we show the calculated change in linewidth (FWHM) for both SLMoS$_2$ and BLMoS$_2$ for the relevant doping concentrations in our experiments. The FWHM of the A_{1g} mode increases significantly more than that of the E_{2g}^1 mode for both SLMoS$_2$ and BLMoS$_2$. This clearly indicates strong EPC for the A_{1g} mode, which is in excellent agreement with our experiments. The ratio of the EPC strength at Γ also confirms this conclusion ($\lambda_{A_{1g}}/\lambda_{E_{2g}^1} \approx 10^2$). The computed change in FWHM (~ 1.3 cm^{-1} with GGA) is also in good agreement with our experiment (~ 1.2 cm^{-1}). Since the change in FWHM due to doping can depend on the exchange–correlation functional used, we confirm our conclusions using LDA as well (see ESI†).

We also compute the change in the phonon mode frequencies due to electron doping within the Born–Oppenheimer approximation using DFPT. The electron doping corresponding to different gate voltages is simulated by adding a fraction of electrons in the SLMoS$_2$ unit cell. We find that the A_{1g} mode softens significantly, while the change in the E_{2g}^1 mode frequency is negligible (Fig. 4c). It is well known that the magnitude of the softening can be sensitive to the exchange–correlation used.[37,61] The softening calculated with GGA of ~ 0.3 cm^{-1} (LDA ~ 0.9 cm^{-1}) is underestimated (overestimated, see ESI†) compared with our experimental result of ~ 0.75 cm^{-1} for $\tilde{V}_g = 50$ V. For BLMoS$_2$, we find that the softening of the A_{1g} mode frequency (~ 0.15 cm^{-1}) is marginally lower than that found for SLMoS$_2$ with GGA, consistent with the trends in our experiments. However, this small change is within the accuracy of our calculations.

In order to qualitatively understand the strong (weak) EPC for the A_{1g} (E_{2g}^1) mode, we study the change in the electronic band structure due to frozen atomic displacement corresponding to the phonon mode.[62,63] For SLMoS$_2$, from the Fermi level position for electron doping relevant to our experiments, we conclude that only the K valley near the conduction band minimum (CBM) is populated. We find that the CBM at the K point changes significantly due to the A_{1g} mode, implying strong EPC, whereas it remains practically unchanged due to the E_{2g}^1 mode, implying weak EPC (Fig. 4d). This simple argument can also be easily extended to BLMoS$_2$, confirming our experimental observations.

Quantitative estimates of the softening of the phonon modes and FWHM for different twist angles due to doping are computationally challenging. Nevertheless, the doping dependence of the softening of the A_{1g} mode (single layer-like at large θ, bilayer-like at small θ, Fig. 2f) can be qualitatively understood from the evolution of the interlayer coupling presented earlier. However, the ΔFWHM for $\theta \approx 1°$ (Fig. 2e) saturates at a significantly lower gate voltage than for BLMoS$_2$, which cannot be explained without explicit calculation of EPC and probably suggests band flattening. It is also interesting to note that, at larger electron doping than that considered here, multiple inequivalent valleys might be occupied, which can lead to greater softening of the phonon mode frequencies and superconductivity.[37,61,64–66]

The low-frequency shear and layer breathing modes originate from the relative displacement of the constituent layers in bilayer MoS$_2$ and provide a non-destructive probe for the interlayer coupling.[67–69] Therefore, these low-frequency modes can provide further insights into the evolution of the interlayer coupling strength and can also be used as a sensitive probe for twist angle.[18,19,26] Furthermore, a recent computational study also suggests the existence of phason modes in all twisted bilayer structures.[26] The detection of these phason modes and their twist angle dependent velocity can provide valuable information about the rigidity of the moiré lattices.

4. Conclusions

We have demonstrated the systematic evolution of the interlayer coupling in twisted bilayer MoS$_2$ using Raman spectroscopy. When the twist between the two layers is large, tBLMoS$_2$ behaves like SLMoS$_2$, whereas for small twist angles it behaves like BLMoS$_2$. Furthermore, using doping dependent Raman spectroscopy, we observe strong EPC in the A_{1g} mode irrespective of the number of layers or the twist angle between them, unlike the E_{2g}^1 mode which shows weak EPC. We explain our results by combining classical force field and first principles based simulations. Our study provides another step toward twistnonics[26] and can be generalized to other TMDCs.

Conflicts of interest

There are no conflicts to declare.

References

1 R. Pisoni, Y. Lee, H. Overweg, M. Eich, P. Simonet, K. Watanabe, T. Taniguchi, R. Gorbachev, T. Ihn and K. Ensslin, *Nano Lett.*, 2017, **17**, 5008–5011.

2 Q. H. Wang, K. Kalantar-Zadeh, A. Kis, J. N. Coleman and M. S. Strano, *Nat. Nanotechnol.*, 2012, **7**, 699.

3 X. Cui, G.-H. Lee, Y. D. Kim, G. Arefe, P. Y. Huang, C.-H. Lee, D. A. Chenet, X. Zhang, L. Wang, F. Ye, F. Pizzocchero, B. S. Jessen, K. Watanabe, T. Taniguchi, D. A. Muller, T. Low, P. Kim and J. Hone, *Nat. Nanotechnol.*, 2015, **10**, 534.

4 D. Sarkar, X. Xie, W. Liu, W. Cao, J. Kang, Y. Gong, S. Kraemer, P. M. Ajayan and K. Banerjee, *Nature*, 2015, **526**, 91.

5 K. Roy, M. Padmanabhan, S. Goswami, T. P. Sai, G. Ramalingam, S. Raghavan and A. Ghosh, *Nat. Nanotechnol.*, 2013, **8**, 826.

6 T. Ahmed, M. H. Naik, S. Kumari, S. P. Suman, R. Debnath, S. Dutta, U. V. Waghmare, M. Jain and A. Ghosh, *2D Mater.*, 2019, **6**, 4.

7 M. H. Naik and M. Jain, *Phys. Rev. B*, 2017, **95**, 165125.

8 Y. Cao, V. Fatemi, A. Demir, S. Fang, S. L. Tomarken, J. Y. Luo, J. D. Sanchez-Yamagishi, K. Watanabe, T. Taniguchi, E. Kaxiras, R. C. Ashoori and P. Jarillo-Herrero, *Nature*, 2018, **556**, 80.

9 Y. Cao, V. Fatemi, S. Fang, K. Watanabe, T. Taniguchi, E. Kaxiras and P. Jarillo-Herrero, *Nature*, 2018, **556**, 43.

10 M. Yankowitz, S. Chen, H. Polshyn, Y. Zhang, K. Watanabe, T. Taniguchi, D. Graf, A. F. Young and C. R. Dean, *Science*, 2019, **363**, 1059–1064.

11 A. L. Sharpe, E. J. Fox, A. W. Barnard, J. Finney, K. Watanabe, T. Taniguchi, M. Kastner and D. Goldhaber-Gordon, arXiv preprint arXiv:1901.03520, 2019.

12 W. Yao, E. Wang, C. Bao, Y. Zhang, K. Zhang, K. Bao, C. K. Chan, C. Chen, J. Avila, M. C. Asensio, J. Zhu and S. Zhou, *Proc. Natl. Acad. Sci. U. S. A.*, 2018, **115**, 6928–6933.

13 K. Kim, S. Coh, L. Z. Tan, W. Regan, J. M. Yuk, E. Chatterjee, M. Crommie, M. L. Cohen, S. G. Louie and A. Zettl, *Phys. Rev. Lett.*, 2012, **108**, 246103.

14 R. W. Havener, H. Zhuang, L. Brown, R. G. Hennig and J. Park, *Nano Lett.*, 2012, **12**, 3162–3167.

15 S. Huang, X. Ling, L. Liang, J. Kong, H. Terrones, V. Meunier and M. S. Dresselhaus, *Nano Lett.*, 2014, **14**, 5500–5508.

16 M.-L. Lin, Q.-H. Tan, J.-B. Wu, X.-S. Chen, J.-H. Wang, Y.-H. Pan, X. Zhang, X. Cong, J. Zhang, W. Ji, P.-A. Hu, K.-H. Liu and P.-H. Tan, *ACS Nano*, 2018, **12**, 8770–8780.

17 K. Liu, L. Zhang, T. Cao, C. Jin, D. Qiu, Q. Zhou, A. Zettl, P. Yang, S. G. Louie and F. Wang, *Nat. Commun.*, 2014, **5**, 4966.

18 S. Huang, L. Liang, X. Ling, A. A. Puretzky, D. B. Geohegan, B. G. Sumpter, J. Kong, V. Meunier and M. S. Dresselhaus, *Nano Lett.*, 2016, **16**, 1435–1444.

19 A. A. Puretzky, L. Liang, X. Li, K. Xiao, B. G. Sumpter, V. Meunier and D. B. Geohegan, *ACS Nano*, 2016, **10**, 2736–2744.

20 S. Zheng, L. Sun, X. Zhou, F. Liu, Z. Liu, Z. Shen and H. J. Fan, *Adv. Opt. Mater.*, 2015, **3**, 1600–1605.

21 X. Zhang, R. Zhang, Y. Zhang, T. Jiang, C. Deng, X. Zhang and S. Qin, *Opt. Mater.*, 2019, **94**, 213–216.

22 A. M. van Der Zande, J. Kunstmann, A. Chernikov, D. A. Chenet, Y. You, X. Zhang, P. Y. Huang, T. C. Berkelbach, L. Wang, F. Zhang, M. S. Hybertsen, D. A. Muller, D. R. Reichman, T. F. Heinz and J. C. Hone, *Nano Lett.*, 2014, **14**, 3869–3875.

23 M. H. Naik and M. Jain, *Phys. Rev. Lett.*, 2018, **121**, 266401.

24 S. Zhu and H. T. Johnson, *Nanoscale*, 2018, **10**, 20689–20701.

25 P.-C. Yeh, W. Jin, N. Zaki, J. Kunstmann, D. Chenet, G. Arefe, J. T. Sadowski, J. I. Dadap, P. Sutter, J. Hone and R. M. Osgood, *Nano Lett.*, 2016, **16**, 953–959.

26 I. Maity, M. H. Naik, P. K. Maiti, S. Ramaswamy, H. Krishnamurthy and M. Jain, arXiv preprint arXiv:1905.11538, 2019.

27 F. Wu, T. Lovorn, E. Tutuc, I. Martin and A. MacDonald, *Phys. Rev. Lett.*, 2019, **122**, 086402.

28 M. Fleischmann, R. Gupta, S. Sharma and S. Shallcross, arXiv preprint arXiv:1901.04679, 2019.

29 M. H. Naik, S. Kundu, I. Maity and M. Jain, arXiv preprint arXiv:1908.10399, 2019.

30 N. Lu, H. Guo, Z. Zhuo, L. Wang, X. Wu and X. C. Zeng, *Nanoscale*, 2017, **9**, 19131–19138.

31 Y. Tan, F. W. Chen and A. W. Ghosh, *Appl. Phys. Lett.*, 2016, **109**, 101601.

32 K. Zhou, D. Wickramaratne, S. Ge, S. Su, A. De and R. K. Lake, *Phys. Chem. Chem. Phys.*, 2017, **19**, 10406–10412.

33 B. Radisavljevic and A. Kis, *Nat. Mater.*, 2013, **12**, 815.

34 A. Das, S. Pisana, B. Chakraborty, S. Piscanec, S. K. Saha, U. V. Waghmare, K. S. Novoselov, H. R. Krishnamurthy, A. K. Geim, A. C. Ferrari and A. K. Sood, *Nat. Nanotechnol.*, 2008, **3**, 210.

35 S. Pisana, M. Lazzeri, C. Casiraghi, K. S. Novoselov, A. K. Geim, A. C. Ferrari and F. Mauri, *Nat. Mater.*, 2007, **6**, 198.

36 B. Chakraborty, A. Bera, D. Muthu, S. Bhowmick, U. V. Waghmare and A. Sood, *Phys. Rev. B: Condens. Matter Mater. Phys.*, 2012, **85**, 161403.

37 E. Ponomarev, T. Sohier, M. Gibertini, H. Berger, N. Marzari, N. Ubrig and A. F. Morpurgo, arXiv preprint arXiv:1901.08012, 2019.

38 X. Lu, M. Utama, X. Wang, W. Xu, W. Zhao, M. H. S. Owen and Q. Xiong, *Small*, 2017, **13**, 1701039.

39 W. M. Parkin, A. Balan, L. Liang, P. M. Das, M. Lamparski, C. H. Naylor, J. A. Rodríguez-Manzo, A. C. Johnson, V. Meunier and M. Drndic, *ACS Nano*, 2016, **10**, 4134–4142.

40 H. Li, J. Wu, Z. Yin and H. Zhang, *Acc. Chem. Res.*, 2014, **47**, 1067–1075.

41 K. S. Novoselov, D. Jiang, F. Schedin, T. Booth, V. Khotkevich, S. Morozov and A. K. Geim, *Proc. Natl. Acad. Sci. U. S. A.*, 2005, **102**, 10451–10453.

42 K. S. Novoselov, A. K. Geim, S. V. Morozov, D. Jiang, Y. Zhang, S. V. Dubonos, I. V. Grigorieva and A. A. Firsov, *Science*, 2004, **306**, 666–669.

43 Y. Guo, C. Liu, Q. Yin, C. Wei, S. Lin, T. B. Hoffman, Y. Zhao, J. Edgar, Q. Chen, S. P. Lau, J. Dai, H. Yao, H.-S. P. Wong and Y. Chai, *ACS Nano*, 2016, **10**, 8980–8988.

44 S. Plimpton, *J. Comput. Phys.*, 1995, **117**, 1–19.

45 J.-W. Jiang, *Nanotechnology*, 2015, **26**, 315706.

46 M. H. Naik, I. Maity, P. K. Maiti and M. Jain, *J. Phys. Chem. C*, 2019, **123**(15), 9770–9778.

47 A. Togo and I. Tanaka, *Scr. Mater.*, 2015, **108**, 1–5.

48 W. Kohn and L. J. Sham, *Phys. Rev.*, 1965, **140**, A1133.

49 P. Hohenberg and W. Kohn, *Phys. Rev.*, 1964, **136**, B864.

50 P. Giannozzi, S. Baroni, N. Bonini, M. Calandra, R. Car, C. Cavazzoni, D. Ceresoli, G. L. Chiarotti, M. Cococcioni, I. Dabo, A. D. Corso, S. de Gironcoli, S. Fabris, G. Fratesi, R. Gebauer, U. Gerstmann, C. Gougoussis, A. Kokalj, M. Lazzeri, L. Martin-Samos, N. Marzari, F. Mauri, R. Mazzarello, S. Paolini, A. Pasquarello, L. Paulatto, C. Sbraccia, S. Scandolo, G. Sclauzero, A. P. Seitsonen, A. Smogunov, P. Umari and R. M. Wentzcovitch, *J. Phys.: Condens. Matter*, 2009, **21**, 395502.

51 D. Hamann, *Phys. Rev. B: Condens. Matter Mater. Phys.*, 2013, **88**, 085117.

52 S. Grimme, *J. Comput. Chem.*, 2006, **27**, 1787–1799.

53 N. Marzari, A. A. Mostofi, J. R. Yates, I. Souza and D. Vanderbilt, *Rev. Mod. Phys.*, 2012, **84**, 1419.

54 A. A. Mostofi, J. R. Yates, Y.-S. Lee, I. Souza, D. Vanderbilt and N. Marzari, *Comput. Phys. Commun.*, 2008, **178**, 685–699.

55 F. Giustino, M. L. Cohen and S. G. Louie, *Phys. Rev. B: Condens. Matter Mater. Phys.*, 2007, **76**, 165108.

56 S. Poncé, E. R. Margine, C. Verdi and F. Giustino, *Comput. Phys. Commun.*, 2016, **209**, 116–133.

57 C. Lee, H. Yan, L. E. Brus, T. F. Heinz, J. Hone and S. Ryu, *ACS Nano*, 2010, **4**, 2695–2700.

58 A. Molina-Sanchez and L. Wirtz, *Phys. Rev. B: Condens. Matter Mater. Phys.*, 2011, **84**, 155413.

59 L. Liang, A. A. Puretzky, B. G. Sumpter and V. Meunier, *Nanoscale*, 2017, **9**, 15340–15355.

60 F. Caruso, M. Hoesch, P. Achatz, J. Serrano, M. Krisch, E. Bustarret and F. Giustino, *Phys. Rev. Lett.*, 2017, **119**, 017001.

61 D. Novko, arXiv preprint arXiv:1907.04766, 2019.

62 J. Bardeen and W. Shockley, *Phys. Rev.*, 1950, **80**, 72.

63 F. Khan and P. Allen, *Phys. Rev. B: Condens. Matter Mater. Phys.*, 1984, **29**, 3341.

64 E. Piatti, D. De Fazio, D. Daghero, S. R. Tamalampudi, D. Yoon, A. C. Ferrari and R. S. Gonnelli, *Nano Lett.*, 2018, **18**, 4821–4830.

65 Y. Ge and A. Y. Liu, *Phys. Rev. B: Condens. Matter Mater. Phys.*, 2013, **87**, 241408.

66 D. Costanzo, S. Jo, H. Berger and A. F. Morpurgo, *Nat. Nanotechnol.*, 2016, **11**, 339.

67 I. Maity, P. K. Maiti and M. Jain, *Phys. Rev. B*, 2018, **97**, 161406.

68 Y. Zhao, X. Luo, H. Li, J. Zhang, P. T. Araujo, C. K. Gan, J. Wu, H. Zhang, S. Y. Quek, M. S. Dresselhaus and Q. Xiong, *Nano Lett.*, 2013, **13**, 1007–1015.

69 L. Liang, J. Zhang, B. G. Sumpter, Q.-H. Tan, P.-H. Tan and V. Meunier, *ACS Nano*, 2017, **11**, 11777–11802.